X-Ray-Imaging Spectrometer (XRIS) for studies of residual kinetic energy and low-mode asymmetries in Inertial Confinement Fusion implosions at OMEGA (invited)

P. J. Adrian,[1, a)] B. Bachmann,[2] R. Betti,[3] A. Birkel,[4] P. Heuer,[3] M. Gatu Johnson,[4] N. V. Kabadi,[4] J. P. Knauer,[3] J. Kunimune,[4] C. K. Li,[4] O. M. Mannion,[5] R. D. Petrasso,[4] S. P. Regan,[3] H. G. Rinderknecht,[3] C. Stoeckl,[4] F.H. Séguin,[4] A. Sorce,[3] R. C. Shah,[3] G. D. Sutcliffe,[4] and J. A. Frenje[4]

[1)] *Plasma Science and Fusion Center: MIT, Cambridge, MA 02139*

[2)] *Lawrence Livermore National Laboratory, Livermore, California 94550*

[3)] *Laboratory for Laser Energetics: University of Rochester, Rochester, NY 14623*

[4)] *Plasma Science and Fusion Center: MIT, Cambridge, MA 02139*

[5)] *Sandia National Laboratories, Albuquerque, New Mexico, USA*

(Dated: 24 May 2022)

A system of x-ray imaging spectrometers (XRIS) has been implemented on the OMEGA Laser Facility capable of spatially- and spectrally-resolving x-ray self-emission from 5-40 keV. The system consists of three independent imagers with nearly-orthogonal lines of sight for 3D reconstructions of the x-ray emission region. The distinct advantage of the XRIS system is its large dynamic range enabled by the use of tantalum apertures with radii ranging from 50 μm to 1 mm, magnifications of 4 to 35x, and image plates with any filtration level. In addition, XRIS is capable of recording 1-100's of images along a single line of sight facilitating advanced statistical inference on the detailed structure of the x-ray emitting regions. Properties such as P0 and P2 of an implosion are measured to 1% and 10% precision respectively. Furthermore, the T_e can be determined to 5% accuracy. Lastly, a spatial measurement of the x-ray emission from XRIS has been used simultaneously with temporally-resolved measurements form the Particle X-ray Temporal Diagnostic (PXTD) to reconstruct the dynamics of x-ray emission during an experiment.

I. INTRODUCTION

Inertial Confinement Fusion (ICF) implosion designs accelerate a deuterium-tritium (DT) ice shell inwards via laser ablation to compress a low-density DT gas at the center to ignition conditions[1]. The low-density gas forms a hot spot which propagates a burn wave into the surrounding high-density fuel. These implosions routinely create burning plasmas at the National Ignition Facility (NIF) where alpha particle heating is exceeding the heating due to mechanical work by the imploding shell[2,3]. Controlling degradation mechanisms such as low-mode asymmetry of the shell and mixing of hot spot and shell are critical to implosion performance[4]. Low-mode asymmetry of the shell causes inefficient conversion of shell kinetic energy to hot-spot kinetic energy which greatly limits performance. Mixing between the hot spot and shell is generated by shell instabilities, target defects, and engineering features that limit performance through increased radiation losses[5–7].

X-ray imaging spectroscopy is a critical diagnostic technique to diagnose implosion performance through measurements of hot-spot temperature, shape, and mix level[5,8–10]. For example, x-ray spectral measurements are used to measure the thermal electron temperature of the hot spot, T_e[5,8,10]. Previous studies have diagnosed residual kinetic energy in the hot spot by comparing T_e measurements to ion temperature measurements, T_{DT}, made with neutron time-of-flight (nTOF) detectors[10]. In addition, x-ray imaging diagnoses the overall shape of the hot spot, which is used to empirically control the drive asymmetry on different ICF platforms. Furthermore, localized bright regions are routinely seen in x-ray self-emission images[11]. The bright regions are generated from the injection of outside material into the hot spot. X-ray imaging spectroscopy provides spatially resolved T_e measurements that have shown these localized bright emission regions to be cooler than the surrounding hot spot[5].

X-ray penumbral imaging is the standard imaging technique used in x-ray imaging spectroscopy. Penumbral imaging is a coded imagining technique where the size of the aperture, D, is larger than the emitting source size, r_S ($D > r_S$). The recorded penumbral image, P, consists of an umbra and penumbra. The umbra region of differentially filtered images is typically used to measure the total emitted x-ray brightness and a spatially averaged, T_e[8]. The penumbral region contains all the infor-

[a)] Author to whom correspondence should be addressed:pjadrian@mit.edu

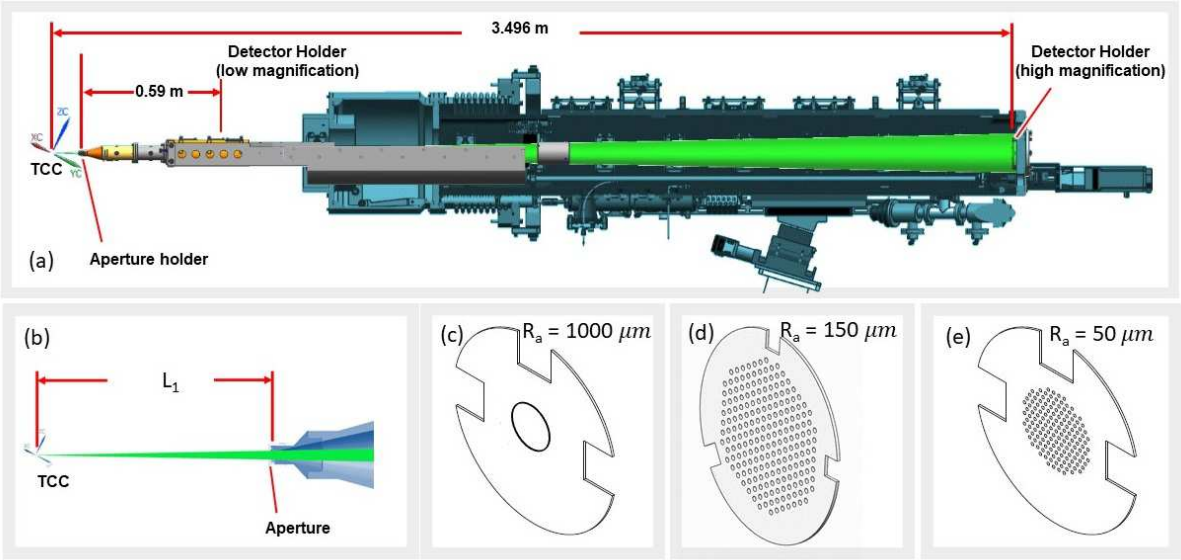

FIG. 1. Schematic of XRIS hardware. (a) Full schematic of XRIS in an OMEGA Ten-inch Manipulator (TIM) insertion module. The farthest detector holder (high magnification) is positioned at the back end of the TIM at 3.496 m from Target Chamber Center (TCC). The second in-close detector holder (low magnification) is positioned at a distance 0.59 m from the aperture. (b) Zoom-in of the aperture holder, which positions an aperture a variable distance, L_1, from TCC. (c) A single R_a=1000μm aperture. (d) An array of 212 apertures with R_a=150μm. (e) An array of 151 apertures with R_a=50μm.

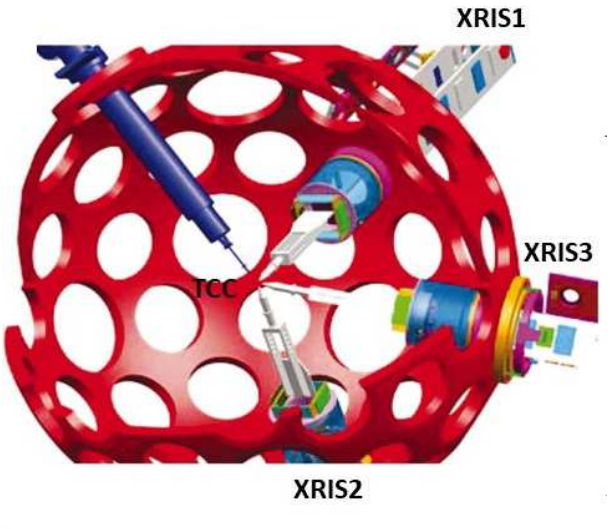

FIG. 2. Drawing of three XRIS systems in nearly orthogonal lines of sight on OMEGA.

mation about the source distribution. Penumbral imaging is attractive because it can work at lower photon yields and possesses higher signal-to-noise as compared to pinhole imaging under certain conditions[9]. In addition, the penumbral image contains redundancy and thus is resistant to single pixel corruption, unlike pinhole imaging.

This work describes the implementation and use of the X-ray Imaging Spectrometer (XRIS) on OMEGA[12], and resulting data obtained. XRIS can be operated in multiple configurations specialized to the experiment. This work describes upgrades to the hardware, which enable 35x magnification. This high magnification mode of XRIS enables imaging with spatial resolutions down to the diffraction limit of the aperture. Furthermore, XRIS can be operated with three nearly orthogonal lines of sight enabling the 3D structure of the hot spot to be probed. In addition, XRIS is a perfect complement to the phase-2 Particle X-ray Temporal Diagnostic (PXTD-2)[1314], which is used to measure time resolved x-ray emission histories in different energy bands. The x-ray emission imaged with XRIS combined with the time resolved PXTD provides a dynamic picture of x-ray emission dynamics from the hot spot.

The structure of this paper is as follows. Section II describes the XRIS hardware and implementation. Section III describes different 2D reconstruction routines and contrasts their performance. Section III discusses the different measurements possible with the different XRIS configurations. Section IV concludes and details future plans with XRIS.

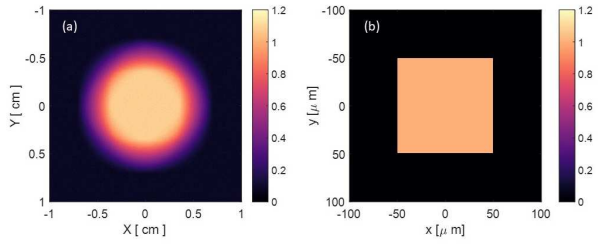

FIG. 3. (a) Penumbral image used in synthetic data study. (b) Brightness profiles used to generate penumbral image in (a).

II. XRIS HARDWARE

XRIS is fielded by TIMs, which holds the penumbral aperture at various stand-off distances from the implosion and houses the image plate detectors. Figure 1(a) displays the full XRIS diagnostic as it is housed in the TIM enclosure. The image-plate detector can be fielded in two locations, one for low magnification and one for high magnification.

The low-magnification configuration positions the detector in an enclosure that extends into the OMEGA target chamber and is fixed at a distance of 0.59 m away from the location of the aperture. This configuration is used for an older version of the imaging system discussed in Ref 15–17. The upper limit of the magnification for the low magnification configuration is set by the standoff distance from target to aperture. Generally, an aperture can be fielded up to 4 cm away from the implosions enabling magnifications up to $M = 59/4 = 14.75\times$. The detection area for this configuration is a 7 cm diameter region.

Recently implemented was the ability to use a high magnification detector, which is positioned at the back end of the TIM at a distance of 3.496 m from TCC. The detector area is 10×10 cm. The high magnification detector is primarily used for x-ray imaging of cryogenic layered DT implosions. The cryostat hardware that cools the capsule limits the minimum target to aperture distance to about 10 cm at OMEGA. Thus, the high magnification detector images at a magnification of M≈35× for cryogenic targets. At this magnification the spatial resolution of the detector is primarily dictated by blurring due to x-ray diffraction[9].

XRIS is routinely run along multiple lines-of-sight for diagnosing implosions at OMEGA. Figure 2 shows the orientation of the three lines of sight of XRIS in the OMEGA target chamber. XRIS 1, 2, and 3 were run in TIMs 2, 4, and 5, respectively. The angle between each pair of TIMS is about 90^o. Obtaining orthographic projections is critical for 3D reconstructions of the x-ray emission.

Three types of apertures are commonly used in XRIS. The first aperture is a single 1000 μm radius aperture shown in Fig. 1(c). This large aperture guarantees that $D > r_S$ for most typical implosions at OMEGA. The second aperture consists of an array of 212 apertures with 150 μm radius (Fig. 1(d)). The third aperture consists of an array of 151 apertures with radii of 50 μm (Fig. 1(e)). This design was intended for small source sizes with faint signals. The use of an aperture array allows for many images to be collectively analyzed to substantially improve signal to noise.

XRIS runs with Fuji ^{TM} image plates as the detector[18]. The kinematic bases for both the low and high magnification detectors allow for multiple image plates and filters to be fielded. XRIS is also capable of running with other solid state detectors, such as CR39. The CR39 is used to detect charged particles generated from an implosion that pass through the apertures. This capability is routinely utilized to image MeV-energy dueterons generated from the elastic scattering of 14.1 MeV neutrons with the deuterium in the dense shell in cryogenic DT implosions at OMEGA[1920]. The XRIS hardware is routinely used to image both x-ray emission and elastically scattered charged particles from layered-cryogenic DT implosions at OMEGA.

III. RECONSTRUCTION TECHNIQUES AND PERFORMANCE

Penumbral imaging of x-rays is equivalent to parallel beam projection tomography if the distance between source and aperture is much greater that the size of the source (paraxial approximation) and the attenuation of the x-ray is negligible in the source[21]. With this set of constraints, the penumbral image, P, recorded by a detector is a convolution of the brightness profile, B, and the aperture point spread function, A,

$$P(X,Y) = B(X,Y) * A(X,Y) \tag{1}$$

where X and Y are the Cartesian coordinates in the detector plane. The coordinates in the source plane are x = X/M and y = Y/M. For a hard-edge aperture of radius R_{app} the point spread function is

$$A(X,Y) = \begin{cases} 1, X^2 + Y^2 \leq R_0^2 \\ 0, \text{otherwise,} \end{cases} \tag{2}$$

where $R_0 = R_{app}(M+1)$. The surface brightness, B is a line integral through the emissivity function, S, such that

$$B(x,y) = \int_{-\infty}^{\infty} S(x,y,z)dz, \tag{3}$$

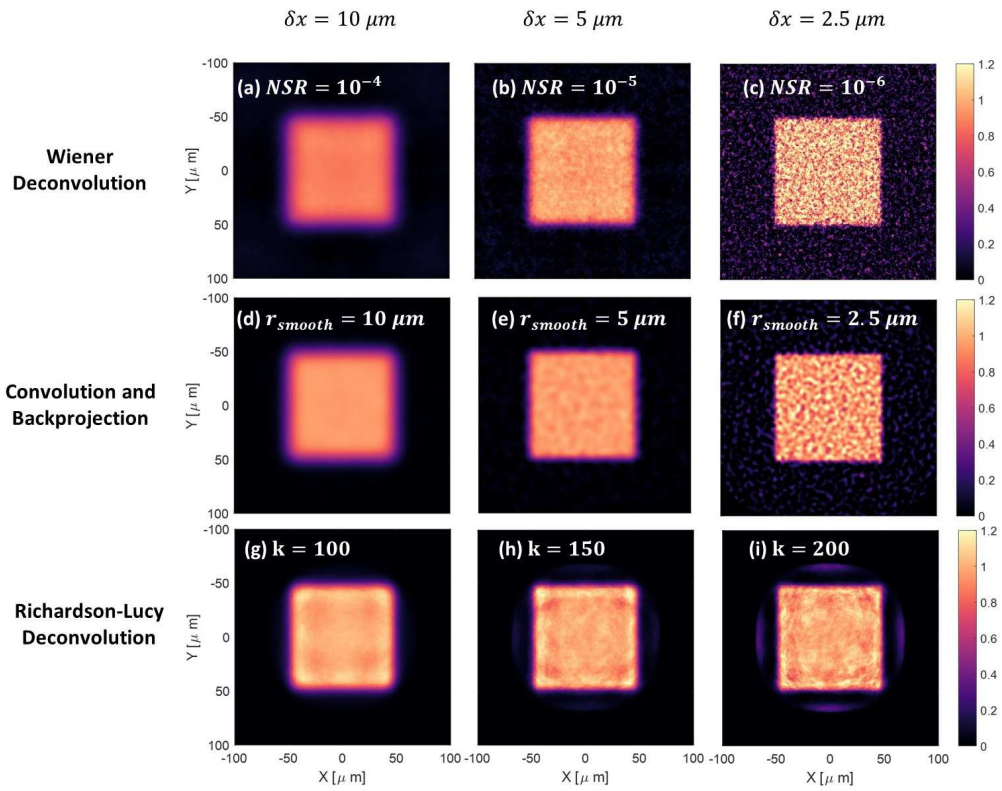

FIG. 4. Reconstructed surface brightness images using the three discussed reconstruction algorithms using the penumbral image shown in Figure 3(a). Panels (a), (b), and (c) display the Wiener deconvolution results for NSR values of 1×10^{-4}, 1×10^{-5}, and 1×10^{-6}, respectively. Panels (d), (e), (f) display the convolution and backprojection results for r_{smooth} values of 10 μm, 5 μm, and 2.5 μm, respectively. Panels (g), (h), (i) display the Richardson-Lucy results for iteration k values of 100, 150, and 200, respectively. The columns represent a reconstruction done to a spatial resolution, $\delta x = 10$, 5 ,2 μm from left to right.

where the z direction is taken to be the imaging direction.

A method to deconvolve A from P is required to obtain B. The most direct way is to compute B from Fourier transforms of P and A,

$$B = \mathcal{F}^{-1}\left[\frac{\mathcal{F}[P]}{\mathcal{F}[A]}\right] \tag{4}$$

where $\mathcal{F}$ and $\mathcal{F}^{-1}$ are the Fourier and inverse Fourier transform. However, Equation 4 can rarely be used with real data because it is extremely sensitive to noise and finite counting statistics. In practice, image reconstruction is performed with special algorithms to the deconvolution problem.

A. Wiener Deconvolution

Wiener deconvolution is a popular method to use as it can deal with the noise problems inherent to Fourier-transform methods of deconvolution[22]. A strength of the Wiener deconvolution method is that information about the spectral-noise content is included into the deconvolution. For white noise the Wiener deconvolution is

$$B = \mathcal{F}^{-1}\left[\frac{\mathcal{F}[P]}{\mathcal{F}[A]}\frac{\mathcal{F}[A]^2}{\mathcal{F}[A]^2 + NSR}\right], \tag{5}$$

where NSR is the total noise to signal power ratio. Generally, NSR is not *a priori* known in penumbral imaging and difficult to quantify from raw data. X-ray penumbral imaging with imaging plates poses multiple sources of noise due to finite photon statistics, neutron hits, and micro scratches in the phosphor layer of the image plate. Therefore, the NSR in practice is a fitting parameter which controls the attenuation of high spatial frequency content in a reconstructed image.

B. Convolution and backprojection

The XRIS images tomographic cords across the image plane enabling the use of convolution and back-projection methods of computed tomography (CT). These backprojection methods have been used in both x-ray and charged particle penumbral imaging[9,15–17]. The back-projection method leverages the Fourier convolution theorem and Fourier-slice theorem to relate B to the radial derivative of P as

$$B = \mathcal{R}^{-1}\left[\frac{dP(X-R_0, Y-R_0)}{dR}\right] \quad (6)$$

where $\mathcal{R}^{-1}[]$ is the inverse-Radon transform and $R = \sqrt{X^2+Y^2}$. However, the back-projection method is only applicable if $R_{app} \ll r_S$. Seguin *et al.*[23] developed a back projection method which corrects for the circularity of the aperture when $R_{app} \sim r_S$. In Seguin's method B is computed as

$$B \approx \int_0^{2\pi} wP'\Big(R' - M(x\ cos\phi + y\ sin\phi), \phi\Big)d\phi \quad (7)$$

where

$$w = 1 - M(x\ cos\phi + y\ sin\phi) \quad (8)$$

$$R' = \sqrt{R_0^2 - M^2(x\ cos\phi + y\ sin\phi)^2} \quad (9)$$

$$P'(R,\phi) = -\frac{1}{2\pi}C(r)\frac{dP^\star(R,\phi)}{dR} \quad (10)$$

$$P^\star = P * F_{smooth} * F_{CT}. \quad (11)$$

The function $C(r)$ is defined by Eq. (7) in Ref 23. In this algorithm, the penumbral image, P, is both smoothed and filtered through convolution with $F_{smooth} = \exp(-(r/\sqrt{2}r_{smooth})^2)$ and F_{CT} where $F_{CT}(r)$ is the ramp filter defined by $\mathcal{F}(F_{CT}) = |k|$. Here, r_{smooth} is a free parameter that sets the spatial resolution of the reconstruction.

C. Richardson-Lucy Deconvolution

Another popular deconvolution method is the Richardson-Lucy (RL) method[24,25]. This method is a gradient-descent method which finds the maximum-likelyhood solution of Equation 1. The RL method is widely used in astronomy because it can handle Poission statistics when imaging weak signals[26,27]. Furthermore, it forces the surface brightness to be non-negative and preserves the total number of counts comprising the image. The RL algorithm is iterative where the 'k+1' iteration is

$$B_{k+1} = B_k\left[A\frac{P}{A * B_k}\right]. \quad (12)$$

The iteration can be started by starting with an initial guess of B_1 for the image which can be a flat field brightness profile. The RL method is slow requiring many iterations to minimize the mean-squared-error of the model compared to measurement. Therefore, acceleration methods have been pursued to speed up the RL method. This work uses the acceleration method proposed by Ref [28].

D. Reconstruction algorithm performance

All reconstruction methods presented above amplify noise in the reconstructed image and have free parameters which impact the quality of the reconstructed surface brightness. It is critical to understand the spatial resolution and noise amplification of each reconstruction algorithm. The back-projection method is unique because its free parameter, r_{smooth}, sets the amount of spatial blurring in the final reconstruction. However, there is no obvious significance to the number of iterations of the RL deconvolution nor the NSR of the Wiener deconvolution. Furthermore, interpreting a reconstructed surface brightness requires understanding the mapping of noise and background from the penumbral image and of the surface brightness. Numerical studies using synthetic penumbral images are used to address these problems below.

Figure 3(a) shows a penumbral image generated from the convolution of a square surface brightness (Fig. 3(b)) and a circular aperture. The image in Fig. 3(a) was generated at magnification of 35× using a $R_{app} = 150$ μm aperture. The penumbral image was normalized such that both penumbral image and the surface brightness had a maximum value of one. The penumbral image was subsequently degraded by adding a uniform background of white noise. The signal to background level was set to 10 with a standard deviation of 0.01. This level of degradation is typical of observations of XRIS data obtained from cryogenic DT implosions at OMEGA.

The surface brightness was subsequently reconstructed from the penumbral image in Fig. 3(a) using the three deconvolution algorithms presented above. Each row in Fig. 4 displays the results from one of the routines, whereas the columns display the spatial resolution, δx, achieved through different parameter choices for each algorithm. The top row of Fig. 3(a) displays the surface brightness obtained with the Wiener deconvolution algorithm for different choices of NSR. This study demonstrates that the choice of NSR sets δx where larger values blur the image. In addition, this algorithm maps the white noise of the penumbra image into high frequency noise. The noise is uniform in amplitude

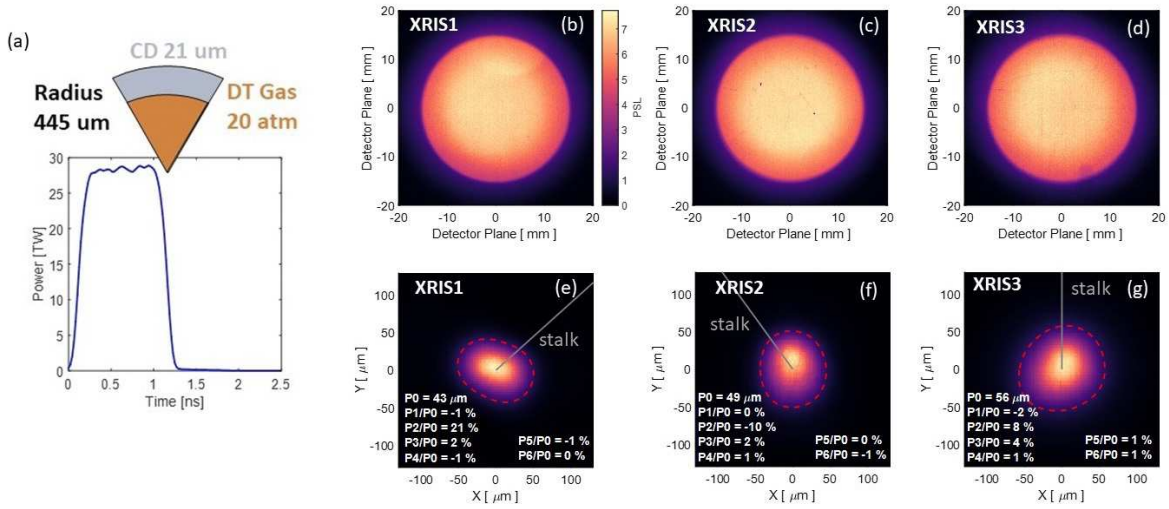

FIG. 5. Sample XRIS data from an ambient DT implosion (shot 96219). (a) depicts the capsule dimensions, fill and laser pulse. Panels (b),(c),and (d) show the raw penumbral images measured from three XRIS systems at nearly orthogonal lines of sight using a $1000\mu m$ radius aperture at magnification 14.5×. Panels (e), (f), and (g) show the reconstructed surface brightness profile from each line of sight.

over the surface brightness. A similar behavior is seen in the performance of the convolution and backprojection algorithm results, which are displayed in the middle row of Fig 4. For this algorithm, the spatial resolution of the resulting surface brightness is simply specified by r_{smooth}. As r_{smooth} decreases a uniform amplitude noise is also observed to degrade the surface brightness reconstruction. However, comparing Fig 4(c) and Fig 4(f), it is observed that the spatial structure of the noise is more 'lumpy' for the backprojection than the Wiener deconvolution. The 'lumpy' nature of the noise is primarily due to the smoothing of the penumbral image in the backprojection method, which excludes high-mode noise from the solution.

Significant deviation in behavior is observed in the results of the RL deconvolution as displayed in the bottom row of Fig. 4. The spatial resolution of the reconstruction decreases as more iterations of the RL algorithm are done. However, the RL algorithm does not map the uniform noise in the penumbral image to uniform noise in the reconstitution, like the Wiener and backprojection algorithms. There is also notably less of high frequency noise in the RL reconstruction than in the two other algorithms. This is apparent in Fig. 4(f) where a significant circular aberration is observed at a radius of ∼60 μm around the square surface brightness profile. The RL algorithm generates this aberration through its positive definite constraint on the reconstruction. As the RL iterates, pixels in the solution that reach zero emission are then excluded from the surface brightness at the next iteration. This builds up groups of dead pixels that cannot be used in the surface brightness. Pixels in the periphery of the image are subsequently used to try to fit noise resulting in the observed aberrations.

Overall, the numerical studies presented in this section are critical for identifying data features in reconstructed surface brightness images and excluding aberrations or noise. However, a remaining challenge is the choice of the free parameters in each algorithm when reconstructing data where the surface brightness is not known. There are no known universal termination conditions for any algorithm. Generally achieving high spatial resolution in the reconstruction comes at the cost of increasing the high-mode noise or introducing spurious aberrations. In this work, data is analyzed with all three algorithms. Numerical studies were done for each configuration of XRIS to determine the spatial resolution set by the three reconstruction algorithms. The reconstruction algorithms were run until they achieved a spatial resolution that was either limited by the pixel size, $\delta x \approx (25\ \mu\ \mathrm{m})/\mathrm{M}$, or x-ray diffraction, $\delta x \approx \sqrt{\lambda L_1}$, where λ is the average x-ray wavelength.

IV. SAMPLE DATA AND ANALYSIS

Example data obtained with different XRIS configurations are shown in this section. All examples used SR-type image plates that were scanned at 25 μm with sensitivity S1000 set by the voltage on the

photo-multiplier tube using the LLE image plate scanner[29]. The fade of each image plate has been corrected based on the shot-to-scan time using fade curves reported in Ref [30].

A. 3D imaging capability

XRIS was fielded in three nearly orthogonal lines of sight using the TIM 2, 4, and 5 to diagnose a DT implosion at OMEGA (shot 96219). Figure 5(a) depicts the capsule dimensions as well as the laser pulse. The implosion was an ambient target with an outer radius of 445 μm filled with 20 atm DT gas in a 21 μm CD shell. The laser pulse was a 1-ns square pulse. Figure 2 shows the orientation of the three lines of sight of XRIS. XRIS was fielded with $50\mu m$ Aluminum and 1500 μm CR39 filters in front of the image plate. Figure 5 (b), (c), and (d) show the measured penumbral images recorded with the $1000\mu m$ aperture at a magnification of 14.5×. The surface brightness was reconstructed from the measured images using the RL algorithm which was iterated until the spatial resolution was estimated to be 6 μm. Figure 5 (e), (f), and (g) display the reconstructed surface brightness along the three nearly-orthogonal lines of sight. In addition, the 17% contour is shown by a dashed red curve in each image along with the P0 through P6 Legendre mode fit of the 17% contour.

Hot-spot volume is a key implosion parameter to diagnose because it is critical to determine the plasma pressure achieved through compression, which is a key performance metric for ignition[31]. The surface brightness images presented in Figure 5 demonstrate the necessity of 3D reconstruction when determining the x-ray emitting volume. 3D low-mode asymmetries prevent accurate volume determination using only one line of sight.

Future work will involve full 3D reconstruction using XRIS data. While there exists mature 3D reconstruction codes for ICF[21], they often invoke an axis of symmetry such as cylindrical symmetry for indirect drive implosions at the NIF. 3D reconstructions at OMEGA will require algorithms, which do not set such constraint.

B. Utilizing multiple penumbral images

Figure 6 displays XRIS data from shot 97587, a cryogenic layered DT implosion with a radius of $466\mu m$ with a $32.7\mu m$ thick ice layer and a $8\mu m$ dueterated polystyrene ablator (CD). Figure 6(a) shows the shaped laser pulse used to implode the capsule. XRIS was run with the $151\times50\mu m$ aperture array using the high magnification detector. The image plate was filtered with 500 μm of Aluminium and 1500 μm of CR39. The recorded penumbral images are shown in Fig 6(b). The magnification was 34.0× and was inferred from the distance between penumbral images recorded in the detector plane.

Each penumbral image is reconstructed independently to obtain the surface brightness. Parallax effects from off-axis apertures in the aperture array are negligible. These effects are of order $1-\cos\beta$ where β is the angle formed between the center penumbral image and the furthest penumbra image. For this detector array, $\beta \approx \arctan(1400\mu m/1.0\times10^5\mu m) \approx 0.8^o$ parallax distortions are of the order $9\times10^{-5} \ll 1$ which is negligible. Figure 6 (c) depicts the surface brightness reconstructed from four different penumbral images enumerated 1, 2, 3 and 4 in Fig 6(b) and (c).

All ∼113 penumbral images in Fig 6(b) were reconstructed to understand statistical variations in the reconstruction of the surface brightness. The source size, $P0$, and mode-2 asymmetry , $P2$, are determined by fitting associated Legendre polynomials to the 17% contour of all images. Figure 7 (a) and (b) displays histograms of the measured P0 and P2, respectively. The variations observed in P0 and P2 are due to noise, photon counting statistics and the variation in penumbral hole size/uniformity. This data demonstrates the P0 and P2 of the hot spot and are determined to 1% and 10% precision, respectively.

C. T_e analysis in multiple lines of sight

Three XRIS systems were fielded using an array of 212 apertures of radii $150\mu m$ TIM 2, 3, and 5 at magnifications 20×, 25×, 35×, respectively. Each XRIS was setup with a detector pack in the high-magnification position consisting of 10 μm Tantulum, 1500 μm CR39, and SR image plate, 250 μm Aluminum, and another SR image plate. The emitted x-ray energy spectra are inferred from the measured x-ray energy deposited on the two differentially filtered penumbral images. Reference 8 details the reconstruction of the x-ray energy spectra including the error analysis. The x-ray spectrum was modeled by using a thermal Bremstrahlung emission profile which scales as $\propto exp(-\hbar\nu/T_e)$, where $\hbar\nu$ is the photon energy. A burn-averaged T_e was inferred using the penumbral images detected on each plate along the different lines of sight. Figure 8 shows the T_e measured in the TIM 2, 3, and 5 lines of sight. As shown in Fig. 8, no line-of sight variations of the electron temperature are observed because the emitted x-rays are unaffected by hot spot bulk mo-

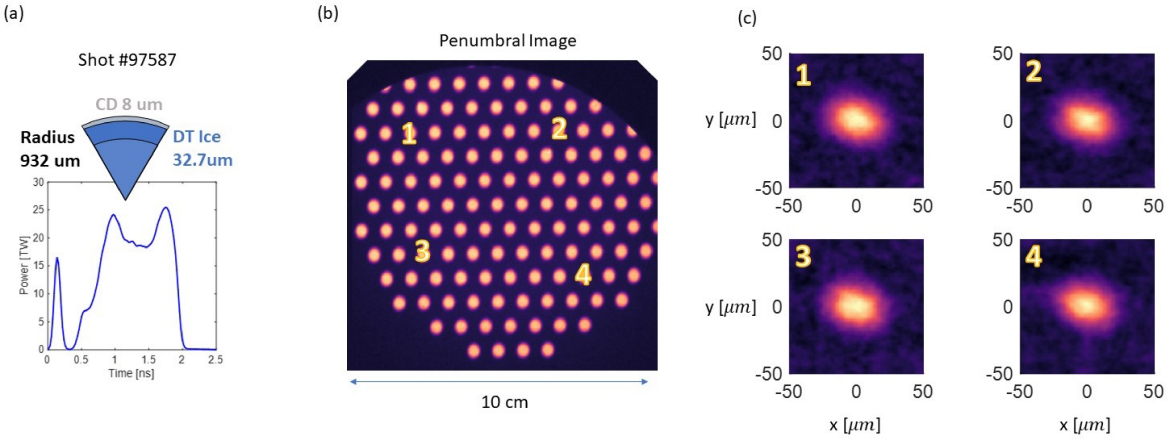

FIG. 6. Sample data from shot 97587. (a) displays the capsule dimensions and composition as well as the laser pulse. (b) Shows the raw penumbral data recorded by XRIS using an aperture array of 50μm radius holes. (c) shows sample reconstructions from individual penumbral images that have been enumerated in the figure.

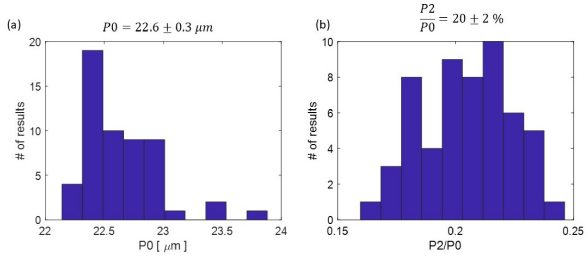

FIG. 7. Inference of P0 = 22.6±0.3 μm (a) and P2 = 20 ± 2 % (b) from the 113 images recorded from shot 97587. The P0 and P@ were determined from the 17% contour of the reconstructed x-ray surface brightness.

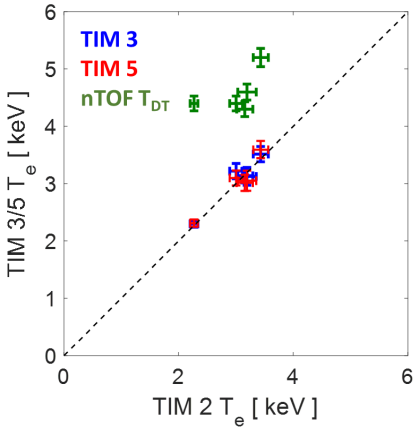

FIG. 8. Burn-averaged T_e measured with XRIS along the TIM 2, 3, and 5 line of sight for a set of five cryogenic DT implosions 102559-102571. For comparison, the DT ion temperature values (green) measured with the 12-meter nTOF system at OMEGA are also shown.

tions which is much slower than the electron thermal speed. In addition, no opacity effects are expected because the x-rays observed have an average energy of 15 keV and are optically thin to the compressed DT-ice layer[32]. However, large differences are observed between the measured T_e and T_{DT}, the latter inferred from the 12-meter neutron rime-of-flight (nTOF) at OMEGA[33]. It is well documented that nTOF inferences of ion temperature are systematically inflated by residual flows which Doppler broaden the DT-neutron energy spectrum[10,34]. The difference between T_e and T_{DT} are currently being studied for direct drive cryogenic layered DT implosions to assess the residual kinetic energy and its sources[32].

D. Simultaneous XRIS and emission-history measurements of implosions at OMEGA

The XRIS system was used simultaneously with the particle/x-ray temporal diagnostic (PXTD), which is capable of measuring x-ray emission histories in multiple energy bands[13,35] to diagnose a series of implosions. Details about the upgraded PXTD are found in Ref 35. The combination of x-ray images and emission histories are a powerful set of data for constraining simulations and models.

Figure 9 displays data taken by XRIS and PXTD for shot 100521 at OMEGA. In this experiment a 484.7 μm radius capsule with a 18.6 μm CH ablator filled with 4.5 atm DT gas was imploded with the laser intensity profile given in Fig 9 (b). The PXTD measured the x-ray emission history of photons with a median energy of $\sim$ 10 keV (black curve in Fig 9

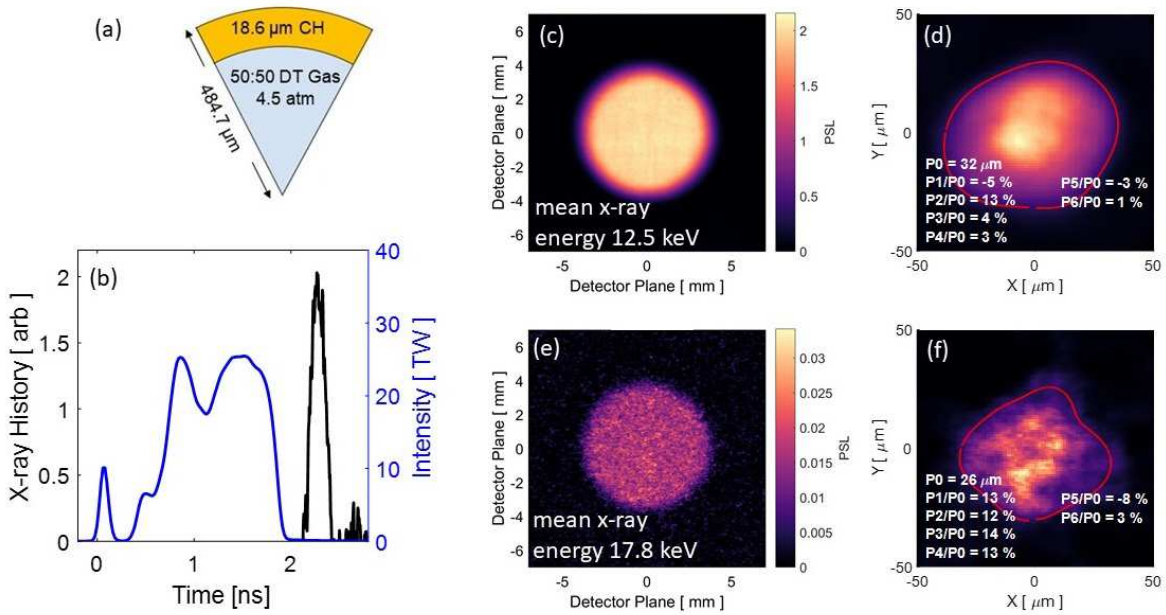

FIG. 9. XRIS and PXTD sample data from shot 100521. (a) Capsule diagram. (b) Time history of the laser pulse (blue) and measured x-ray emission history (black). (c) and (e) X-ray penumbral images recorded by XRIS with mean x-ray energies of 12.5 and 17.8 keV, respectively. (d) and (f) reconstructions of the surface brightness profile from (c) and (e), respectively with 4 μm resolution using the Richardson-Lucy algorithm.

(b)). Simultaneously XRIS was run with an array of 212 apertures with a 150 μm radius. The magnification of XRIS was 25.0×. Two XRIS images are shown in Fig 9 (c) and (e) which were generated by photons with median energy of 12.5 and 17.8 keV, respectively. Fig 9 (d) and (f) display the surface brightness profile reconstructed from the measured images using the LR algorithm to 4-μm resolution.

The data collected by XRIS and PXTD provide a wealth of information including the x-ray burn width, bang-time, burn volume, and electron temperature which can be used to test implosions models. Bayesian inference techniques have been used to quantify the accuracy of implosion models by comparing the models to data obtained with multiple diagnostics[36]. Recently, Ruby *et al.*[37] demonstrated a technique that utilized simultaneous measurements of spatially and temporally resolved x-ray self emission from implosion hot spot to constrain electron heat conduction transport models. Future work will utilize the Bayesian inference technique proposed in Ref 37 to study electron heat conduction with data simultaneously recorded with XRIS and PXTD.

V. CONCLUSIONS AND OUTLOOK

In summary, XRIS is a multi-functional penumbral imaging system that is used to spatially resolve x-ray emission in different energy bands through differential filtering. Each system can be fielded in any TIM on OMEGA for imaging along multiple lines of sight. A high magnification system enabling x-ray imaging down to 3 μm spatial resolution has been developed for implosions that require the OMEGA cryostat. XRIS records multiple images using an array of apertures along a single line of sight enabling statistical inference of hot-spot properties. Properties such as P0 and P2 of an implosion are measured to 1% and 10% precision respectively. XRIS is readily fielded along multiple lines of sight to image the 3D morphology of the hot spot. X-ray compliments a variety of other x-ray diagnostics in use at OMEGA. Furthermore, the T_e can be determined to 5% accuracy.

Future work with XRIS will involve creating a robust 3D reconstruction algorithm. This will enable accurate estimation of implosion properties such as burn volume, which is difficult to diagnose along one line of sight due to 3D-low-mode asymmetries. Further analysis of 3D x-ray emission in different energy bands will help identify mix mechanisms through the analysis of T_e profiles. In addition, combining XRIS with other x-ray diagnostics, such as PXTD, will be critical to building a holistic picture of the hot spot.

VI. ACKNOWLEDGEMENTS

This work was supported by the U.S. Department of Energy NNSA MIT Center-of-Excellence under Contract DE-NA0003868, and by the Laboratory for Laser Energetics under Contract 417532G/UR FAO GR510907, and by National Laser Users Facility under Contract DE-NA0003938. PJA was supported by the DOE NNSA SSGF Fellowship under DE-NA0003960. This report was prepared as an account of work sponsored by an agency of the United States Government. Neither the United States Government nor any agency thereof, nor any of their employees, makes any warranty, express or implied, or assumes any legal liability or responsibility for the accuracy, completeness, or usefulness of any information, apparatus, product, or process disclosed, or represents that its use would not infringe privately owned rights. Reference herein to any specific commercial product, process, or service by trade name, trademark, manufacturer, or otherwise does not necessarily constitute or imply its endorsement, recommendation, or favoring by the United States Government or any agency thereof. The views and opinions of authors expressed herein do not necessarily state or reflect those of the United States Government or any agency thereof.

VII. DATA AVAILABILITY

The data that support the findings of this study are available from the corresponding author upon reasonable request.

[1] J. Lindl, Physics of Plasmas **2**, 3933 (1995).
[2] A. B. Zylstra et al., Nature **601**, 542 (2022).
[3] A. L. Kritcher et al., Nature Physics **18**, 251 (2022).
[4] D. T. Casey et al., Physics of Plasmas **28**, 042708 (2021).
[5] B. Bachmann et al., Physical Review E **101**, 033205 (2020).
[6] T. Ma et al., Review of Scientific Instruments **83**, 10E115 (2012).
[7] M. Gatu Johnson et al., Physics of Plasmas **27**, 032704 (2020).
[8] P. J. Adrian et al., Review of Scientific Instruments **92**, 043548 (2021).
[9] B. Bachmann et al., Review of Scientific Instruments **87**, 11E201 (2016).
[10] L. C. Jarrott et al., Review of Scientific Instruments **87**, 11E534 (2016).
[11] G. A. Kyrala et al., Review of Scientific Instruments **81**, 10E316 (2010).
[12] T. R. Boehly et al., Optics Communications **133**, 495 (1997).
[13] H. Sio et al., Review of Scientific Instruments **87**, 11D701 (2016).
[14] N. V. Kabadi *et al.* '' submitted to Rev. Sci. Instrum. (2022).
[15] F. H. Séguin et al., Review of Scientific Instruments **75**, 3520 (2004).
[16] F. H. Séguin et al., Physics of Plasmas **23**, 032705 (2016).
[17] F. H. Séguin et al., Physics of Plasmas **13**, 082704 (2006).
[18] M. J. Rosenberg et al., Review of Scientific Instruments **90**, 013506 (2019).
[19] J. Kunimue *et al.* Submitted to Phys. of Plasmas (2022).
[20] H. G. Rinderknecht *et al.* Submitted to Rev. Sci. Instrum. (2022).
[21] P. L. Volegov et al., Review of Scientific Instruments **92**, 033508 (2021).
[22] Gonzalez, R. C., and R. E. Woods. Digital Image Processing. Addison-Wesley Publishing Company, Inc., 1992. - Google Search.
[23] F. H. Séguin et al., Review of Scientific Instruments **75**, 3520 (2004).
[24] W. H. Richardson, JOSA **62**, 55 (1972).
[25] L. B. Lucy, The Astronomical Journal **79**, 745 (1974), ADS Bibcode: 1974AJ.....79..745L.
[26] J. Starck, E. Pantin, and F. Murtagh, Publications of the Astronomical Society of the Pacific **114**, 1051 (2002).
[27] R.J. Hanisch, R.L. White, and R.L. Gilliland, Deconvolutions of Hubble Space Telescope Images and Spectra, Deconvolution of Images and Spectra, Ed. P.A. Jansson, 2nd ed., Academic Press, CA, 1997.
[28] D.S.C. Biggs and M. Andrews, Acceleration of iterative image restoration algorithms, Applied Optics, Vol. 36, No. 8, 1997.
[29] G. J. Williams, B. R. Maddox, H. Chen, S. Kojima, and M. Millecchia, Review of Scientific Instruments **85**, 11E604 (2014).
[30] B. R. Maddox et al., Review of Scientific Instruments **82**, 023111 (2011).
[31] S. P. Regan et al., Fusion Science and Technology **73**, 89 (2018).
[32] D. Cao et al., Physics of Plasmas **26**, 082709 (2019).
[33] V. Y. Glebov et al., Review of Scientific Instruments **75**, 3559–3562 (2004).
[34] T. J. Murphy, Physics of Plasmas **21**, 072701 (2014).
[35] N. Kabadi et al., Review of Scientific Instruments **92**, 023507 (2021).
[36] J. Ruby et al., Physical Review Letters **125**, 215001 (2020), Publisher: American Physical Society.
[37] J. J. Ruby, J. A. Gaffney, J. R. Rygg, Y. Ping, and G. W. Collins, Physics of Plasmas **28**, 032703 (2021).